INTERNATIONAL JOURNAL OF HYDROGEN ENERGY XXX (2017) 1–9

Available online at www.sciencedirect.com

ScienceDirect

journal homepage: www.elsevier.com/locate/he

Experimental and thermodynamic evaluation of $La_{1-x}Sr_xMnO_{3\pm\delta}$ and $La_{1-x}Sr_xCo_{1-y}Fe_yO_{3-\delta}$ cathodes in Cr-containing humidified air

Boxun Hu [a,b], *Sridevi Krishnan* [b,c], *Chiying Liang* [a,b], *Su Jeong Heo* [a,b], *Ashish N. Aphale* [a,b], *Rampi Ramprasad* [b,c], *Prabhakar Singh* [a,b,*]

[a] *Center for Clean Energy Engineering, University of Connecticut, USA*
[b] *Department of Materials Science and Engineering, University of Connecticut, USA*
[c] *Institute of Materials Science, University of Connecticut, USA*

ARTICLE INFO

Article history:
Received 5 November 2016
Received in revised form
5 January 2017
Accepted 6 January 2017
Available online xxx

Keywords:
Solid oxide fuel cell
Chromium poisoning
Cathode degradation
Clean energy
First-principles calculations

ABSTRACT

Chemical and structural stability of strontium doped lanthanum manganite (LSM) and lanthanum cobalt ferrite (LSCF) cathodes in Cr-containing humidified air has been studied by a combination of experimental and thermodynamic approaches. During 100 h tests performed in flowing air (3% H_2O) at 1023 K, the electrochemical performance of LSM/yttria doped zirconia (YSZ)/Pt half-cells exhibited a relatively faster degradation in current (I–t) at 0.5 V applied bias than the LSCF/gadolinium-doped ceria (GDC)/Pt half-cells. Cr species from the gas phase deposited predominantly at LSM/YSZ interface while LSCF showed mainly surface deposition throughout the electrode. Raman spectra indicate $SrCrO_4$ formation on the post tested LSCF cathode but not on the post tested LSM cathode. The polarization resistance of the LSM cathode also increased significantly compared to that of the LSCF cathode. A linear programming approach coupled with first-principles thermodynamics suggests that the stoichiometric LSM remains stable and unreacted for the whole range of experimental P_{CrO3} and temperature conditions whereas the formation of $SrCrO_4$ on LSC cathode is energetically favored at 1023 K supporting the experimental findings.

Introduction

Poisoning of cathode from the gaseous chromium species (Cr^{6+}) originating from the cell to cell interconnect (IC) and balance of plants (BoP) materials have been considered as one of major causes for near and long term electrochemical performance degradation in solid oxide fuel cells (SOFC) and electrolysis cells (SOECs) [1–3]. Although the advantages of SOFC power generation systems in terms of modularity of construction, applications in centralized and distributed power generation, fuel flexibility and significantly higher electrical efficiency (chemical to electrical) along with smaller carbon foot print and absence of pollutants are well documented, successful commercialization of the technology requires long term performance stability, and systems reliability [4]. SOECs, operated in the regenerative mode of SOFCs for the production of clean oxygen, hydrogen and syngas fuels by electrolysis of H_2O and CO_2, share similar long term

* *Corresponding author*. 44 Weaver Road, Storrs Mansfield, CT, 06269-5233, USA. Fax: +1 860 486 8378.
E-mail address: prabhakar.singh@uconn.edu (P. Singh).

http://dx.doi.org/10.1016/j.ijhydene.2017.01.040

performance and reliability concerns and challenges for large scale market implementation [5–7]. Performance degradation in the above electrochemical systems is largely associated with the structural and chemical degradation of the electrochemically active components in the stack modules whereas the overall system cost effectiveness is dictated by the cost of bulk and coating materials, processing techniques used and BoP subsystem requirements. Single SOFC cells, consisting of porous fuel electrode (anode), dense electrolyte layer, and porous oxygen electrode (cathode), are connected through electronically conducting interconnects and gas separators in series to form SOFC stacks [8]. Oxygen reduction at the cathode has been considered as the main rate limiting factor to the SOFC electrochemical performance [9,10]. Compared to an undoped $LaMnO_3$ ($LaCoO_3$), A-site doped (alkaline earth) perovskites and interfacial coating offer increased ionic and electronic conductivity for improving electrochemical performance [11,12]. Strontium doped lanthanum manganite (LSM) containing a dispersed phase of yttrium doped zirconia (YSZ) electrolyte is the state-of-the art cathode for SOFC's operating at high-temperatures (>1073 K). Both A and B site doped lanthanum strontium cobalt ferrites (LSCF) have been extensively used as the cathode for intermediate temperature (823–1023 K) SOFCs due to their high mixed ionic and electronic conductivity and excellent thermal and chemical compatibility with gadolinium-doped ceria (GDC) [13]. By lowering operating temperature, inexpensive ferritic stainless steel (Fe–Cr alloy) is used for the ICs and BoP, thus reducing the cost of SOFC power systems.

Both LSM and LSCF cathodes offer excellent structural and chemical stability under SOFC (SOEC) fabrication and operation conditions [14]. The presence of intrinsic impurities (H_2O, CO_2, and SO_x/H_2S) and extrinsic impurities (gaseous Cr species) in air [15–17] leads to the oxide segregation (SrO, MnO_x) [18–21], compound formation ($SrCrO_4$, $SrCO_3$) [22–25], and electrochemical performance degradation during long-term operation [23]. Water vapor in the cathode atmosphere results in the segregation of strontium oxide/hydroxides at the gas–solid interface and formation of lanthanum zirconate at the solid–solid (cathode-electrolyte) interface leading to electrochemical performance degradation of 3–15% during long term operation (100–1000 h) [26]. The degradation, arising solely due to water vapor, can be partially regained by chemical and thermal treatment including an increase in the operating temperature or removal of water from the air stream [27]. Presence of hexavalent gaseous chromium species such as CrO_3, $CrO(OH)_2$ and $CrO_2(OH)_2$, originating from metallic ICs and BoP components, by a water vapor-mediated volatilization [28], leads to the deposition of chromium oxide and chromium containing reaction products at the cathode surface [29]. Combined presence of water (3% H_2O) and chromium vapor in the LSM cathode atmosphere has been reported to accelerate the irreversible degradation of cell electrochemical performance [1]. Sr-enriched surface and interface, as reported above, serves as nuclei for $SrCrO_4$ formation. Presence of Mn^{2+} in the LSM cathode due to P_{O2} gradient under polarization serves as nuclei for Mn-Cr spinel formation [30].

The surface morphological evolution at the LSM and LSCF cathodes, in terms of structural changes and related compound formation, during exposure to water and chromium vapor shows significant differences in terms of cathode surface and cathode/electrolyte interface morphology and chemistry. Under cathodic polarization conditions, for the LSM cathode, presence of chromium was mainly observed at the LSM/YSZ interface with a lower concentration of chromium distributed across the LSM after a single-cell was exposed to a E-Brite interconnect for 100 h [31]. For the LSCF cathode, high chromium deposition was observed near the LSCF cathode surface with decreasing Cr concentration towards the LSCF/GDC interface. Approximately 1.7 μm of solid Cr containing deposits formed on LSCF cathode surface in presence of the metallic interconnect at 1173 K [29]. Trace amounts of Cr and Sr at LSCF surface with 20-nm depth layer was detected in the presence of 2 atom% Cr by *In-situ* X-ray photoelectron spectroscopy (XPS) [32]. The formation of $SrCrO_4$ at the LSCF cathode surface has been confirmed by Raman spectroscopy [33]. Increase in Cr concentration in the cathode inlet gas significantly increases the cathode polarization resistance [34] and operating temperature and chromium vapor pressure are two key factors influencing the chemical reactions between chromium and the cathodes (LSM and LSCF) also termed as "chromium poisoning". This study investigates formation of reaction products between Cr deposits and LSM (LSCF) electrodes under different Cr partial pressures using a thermodynamic analysis approach. Typical experiments are also conducted to examine the results form thermodynamic analysis. The developed thermodynamic model helps predict the stability of LSM and LSCF cathodes in a wide range of operating conditions.

First-principles methods have been used to systematically identify thermodynamically favorable reaction products for multi component systems based on their successful application in multi component hydrogen storage [35] and CO_2 capture [36] systems. Here, we employ a similar approach to identify the decomposition pathway and reaction energetics of $La_{0.75}Sr_{0.25}MnO_3$ and $La_{0.5}Sr_{0.5}CoO_3$ compounds with a representative Cr species at experimental temperatures and pressure conditions.

Experimental and computational analysis

Experimental

Cell fabrication and electrochemical test procedures used in the study have been discussed in earlier publication [26]. LSM/YSZ/Pt and LSCF/GDC/Pt half-cells have been fabricated by screen-printing technique using LSM ($La_{0.80}Sr_{0.20}MnO_{3-x}$) and LSCF ($(La_{0.60}Sr_{0.40})_{0.995}(Co_{0.20}Fe_{0.80})O_{3-x}$) ink pastes obtained from FuelCell Materials. The YSZ and GDC (~185 ± 25 μm) discs were also obtained from FuelCell Materials. Pt gauze, Pt paste, and Pt wires (Alfa Aesar) have been used as current collector and electrical contacts during experimental studies. The fabricated half-cells were subsequently sintered in a furnace at 1473 K for 2 h with a ramp rate of 3 K/min. Electrochemical half-cell tests to evaluate the chromium poisoning of LSM and LSCF cathode have been performed at 1023 K using an experimental test setup shown in Fig. 1.

Please cite this article in press as: Hu B, et al., Experimental and thermodynamic evaluation of $La_{1-x}Sr_xMnO_{3\pm\delta}$ and $La_{1-x}Sr_xCo_{1-y}Fe_yO_{3-\delta}$ cathodes in Cr-containing humidified air, International Journal of Hydrogen Energy (2017), http://dx.doi.org/10.1016/j.ijhydene.2017.01.040

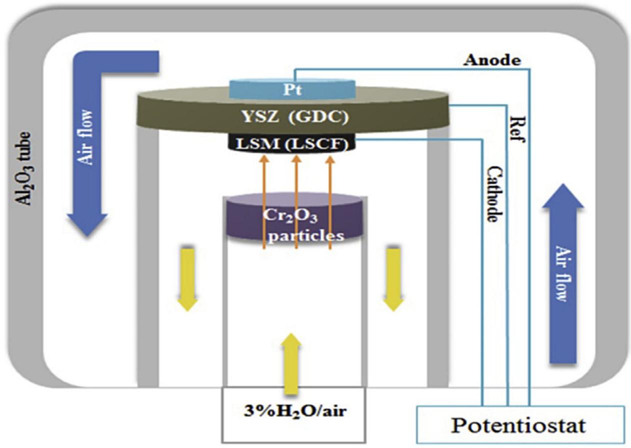

Fig. 1 – Schematic representation of the electrochemical test setup for half-cell performance evaluation. Tests were performed at 1023 K in air-3% H_2O atmosphere.

Electrochemical tests on fabricated half cells (LSM/YSZ/Pt and LSCF/GDC/Pt) were conducted in chromium-vapor (in equilibrium with pure Cr_2O_3) containing wet air (3% H_2O/air) for 100 h at 1023 K. Electrical performance (I–t) as well as chemical analysis for the presence of Cr in the cathode was performed for both cells. Electrochemical performance of the half-cells was measured using a multi-channel potentiostat (VMP2, Bio-Logic). The potentiostat connected the half-cells by three-electrode configuration: LSM (LSCF) cathode, Pt anode, an additional Pt wire connected at the edge of the YSZ (GDC) electrolyte as a reference electrode. The electrochemical impedance spectra (EIS) between the cathode and reference electrode were obtained under a bias of 0.5 V and in the frequency range from 0.5 Hz to 200 kHz with an applied 10 mV sinus amplitude at an interval of 1 h. The morphological and elemental analyses were performed using an FEI Quanta 250 FEG scanning electron microscope (SEM) attached with an energy dispersive X-ray spectroscope (EDS). Raman spectra were recorded on Renishaw System 2000 using a 514 nm excitation line. A Bruker AXS D-8 Advance X-ray diffractometer (XRD) was used for the identification of phases present in both pre- and post-test cells.

Computational analysis

Density functional theory (DFT) is used to study materials at the atomic level. Bulk reaction thermodynamics of SOFC cathodes and CrO_3 system have been studied using first-principles thermodynamics. $La_{0.75}Sr_{0.25}MnO_3$ and $La_{0.5}Sr_{0.5}CoO_3$, considered in the experimental section, were chosen as representatives of the LSM and LSCF cathode materials, respectively. We employed DFT calculations to obtain the ground state energies of various compounds (La, Sr)$MnO_{3-\delta}$ (δ = 0, 0.125), (La, Sr)CoO_3, $Mn_xCr_{3-x}O_4$ (x = 1, 2), $SrCrO_4$, $LaCrO_3$, $CoCr_2O_4$, binary oxides and metals. $La_{0.75}Sr_{0.25}MnO_3$ and $La_{0.5}Sr_{0.5}CoO_3$ were relaxed in the cubic supercell and the ground state structures were considered for the rest of the compounds. Spin polarized calculations are performed using density functional theory as implemented in the VASP code [37]. The exchange correlation is treated using the generalized gradient approximation (GGA) with Perdew–Burke–Ernzerh of exchange-correlation (PBE) function [38]. The projector augmented-wave (PAW) potentials were used to describe the core states. All calculations were performed with a cutoff energy of 520 eV and a high density Monkhorst–Pack k-point grid was used. The atomic positions were relaxed until the force on each atom fell below 0.02 eV/Å.

The energetically most favorable reaction pathway of each of the reactions was obtained using a linear programming (LP) approach. A modified procedure with the involved equations has been reported in earlier publication [39]. The energies of all possible decomposition products of the reaction were introduced into a linear equation with a coefficient. Minimizing these coefficients under the stoichiometry preservation constraints leads to the energetically favorable reaction pathways. The decomposition products in the pool include the elemental metals, their binary oxides, and the doped and undoped parent compounds. In addition, the ternary Cr oxide of each cation involved in the reaction is also included. LP minimization is also repeated for varying concentration of the gaseous Cr species (CrO_3) and for a particular temperature to obtain the free energy as a function of CrO_3 partial pressure. The same procedure is carried out for the temperature range of interest to obtain the phase diagram of reaction energetics.

Results

Electrochemical performance

Fig. 2 shows electrochemical performance of LSM/YSZ/Pt and LSCF/GDC/Pt half-cells in the presence of chromium and water vapor at 1023 K. The LSM/YSZ/Pt half-cell exhibited rapid and large performance degradation in the presence of chromium vapor while the LSCF/GDC/Pt half-cell showed only small performance degradation in the 100 h tests.

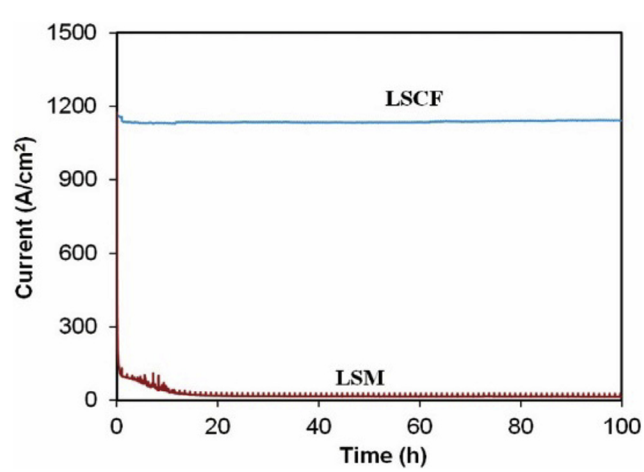

Fig. 2 – I–t curves of LSM/YSZ/Pt and LSCF/GDC/Pt half cells. Tests were conducted at 1023 K with 150 sccm of 3% H_2O/air flowing through a Cr_2O_3 powder bed and an applied bias of 0.5 V.

Please cite this article in press as: Hu B, et al., Experimental and thermodynamic evaluation of $La_{1-x}Sr_xMnO_{3\pm\delta}$ and $La_{1-x}Sr_xCo_{1-y}Fe_yO_{3-\delta}$ cathodes in Cr-containing humidified air, International Journal of Hydrogen Energy (2017), http://dx.doi.org/10.1016/j.ijhydene.2017.01.040

The Nyquist spectra of the LSM and LSCF cathodes, measured by the three-electrode configuration, are shown in Fig. 3. The total resistance of the LSM cathode increased from 5.5 Ω/cm^2 to 30 Ω/cm^2 in 100 h of exposure to chromium-containing air mainly due to increase in polarization resistance. The polarization resistance rapidly increased in the first 20 h and then remained relatively unchanged for the remaining 80 h. Compared to the impedance change of the LSM cathode, the total resistance of the LSCF cathode only increased from 0.59 Ω/cm^2 to 0.63 Ω/cm^2 in 100 h of exposure to chromium-containing air and the small impedance increase was attributed to both increases in polarization and non-polarization resistances.

Surface morphology

Changes in the LSM and LSCF cathode morphology due to the exposure to chromium-containing air are shown in Fig. 4. LSM cathode, exposed to humidified air (3% H_2O/air) shows the formation of a smooth surface without apparent segregation of SrO on the LSM surface. The cathode surface after exposure to chromium-containing 3% H_2O/air for 100 h also remains smooth and clean (Fig. 4B/C) as that of the sample exposed to 3% H_2O/air. The LSCF cathode surface (Fig. 4E/F) after exposure to chromium-containing 3% H_2O/air for 100 h, on the other hand, showed the development of roughness and formation of a thin layer of chromium deposit compared to that of the sample exposed to 3% H_2O/air.

The fracture cross-sections of the cathode and the cathode-electrolyte interface show the emergence of two very different morphologies after exposure to 3% H_2O/air in the presence and absence of chromium (Fig. 5). The LSM cathode shows that the deposition of chromium mostly occurs at the LSM cathode/YSZ electrolyte interface (Fig. 5B). In the case of LSCF cathode, however, the chromium was found to deposit and cover the LSCF cathode surface and preferential segregation was not observed at the interface of the LSCF cathode/GDC surface (Fig. 5D).

Table 1 shows the elemental analyses of cathodes at the cathode surface and cathode/electrolyte interface. For LSM cathode exposed to 3% H_2O/air in the presence of chromium, significant amounts of chromium (~10.8%) is found to accumulate at the interface of the LSM cathode/YSZ electrolyte whereas the LSM cathode surface showed minor increase of approximately 1% Cr. Compared to the results obtained for the LSCF cathode, the presence of Cr on the LSCF cathode surface increased by approximately 10.9% and the cathode/electrolyte interface showed an increase of 1.6%.

Raman spectroscopy technique was used for the identification of surface compounds formed on the cathode surface. Fig. 6 shows the surface of the post tested LSCF cathode with the presence of $SrCrO_4$ with two assigned strong peaks at 867.5 and 893.5 cm^{-1} and small peaks at 378.8 and 406 cm^{-1} [40]. A broad peak between 639 and 689 cm^{-1} was assigned to Co_3O_4 [33]. No such peaks of $SrCrO_4$ were observed on the post tested LSM cathode surface.

DFT calculation

Fig. 7 shows the co-stability of reaction products based on reaction energetics of $La_{0.5}Sr_{0.5}CoO_3$ and $La_{0.75}Sr_{0.25}MnO_3$ with CrO_3 at various P_{CrO3} and temperatures by DFT calculations. The P_{CrO3} in the cathode air stream (with 3% H_2O) at 1023 K is assigned a partial pressure of 0.03×10^{-6} atm [1]. Points p and q highlight the specific boundary and experimental conditions of interest for this study. For the $La_{0.5}Sr_{0.5}CoO_3$ cathode, the study indicates establishment of two reactive (1 and 2) and one non-reactive (3) area under the exposure conditions of interest to SOFC operation. Considering the chemical stability, an LSC cathode can be operated in the temperature range of 900–1300 K and the P_{CrO3} in the cathode flow is in the range of 10^{-10}–10^{-6} atm, which is marked by a blue dashed rectangle in Fig. 7A that includes the reactive area 2 and non-reactive Area 3. In practical applications, LSC cathodes normally work at a low temperature range of 900–1050 K and $P_{CrO3}>10^{-9}$ atm, which is located in the reactive area 2. Based on the reaction energetics, $LaCoO_3$, Co_3O_4, $SrCrO_4$, and O_2 is energetically favored. It is noted that in the half-cell tests on LSCF in chromium containing humidified air, Co_3O_4 and $SrCrO_4$ compounds were observed on the LSCF surface by Raman spectra and SEM-EDS.

For the reaction of $La_{0.75}Sr_{0.25}MnO_3$ cathode to CrO_3, energetics shows the establishment of only a reactive area (4) and a non-reactive area (5) in Fig. 7B. Although the reaction proceeds at higher CrO_3 partial pressure with the formation of Mn_2O_3, $SrCrO_4$, $LaCrO_3$ and O_2 products, the window of operation of interest to SOFC is fully located in the non-reactive Area 5. The bulk reaction energetics suggests that the

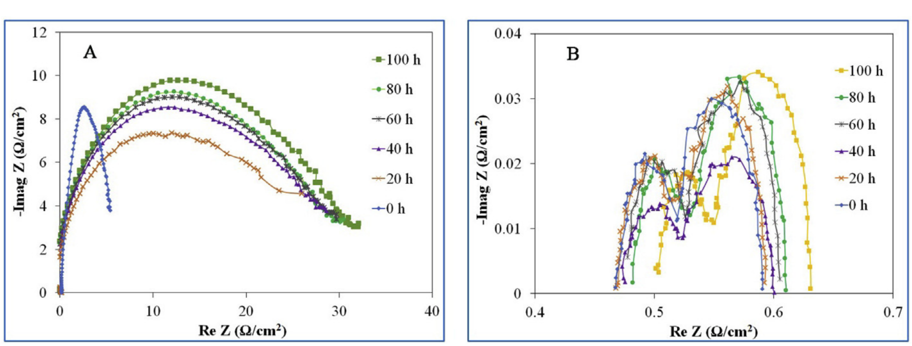

Fig. 3 – EIS spectra of the LSM cathode (A) and LSCF cathode (B) tested at 1023 K with 150 sccm of 3% H_2O/air flowing through a Cr_2O_3 powder bed.

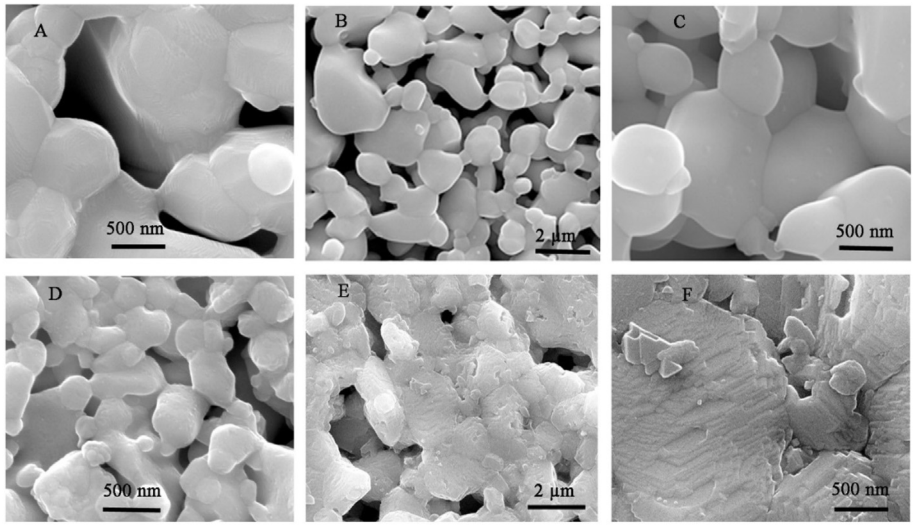

Fig. 4 – Surface morphologies of LSM and LSCF cathode exposed to 3% H_2O/air in the absence and presence of Cr vapor at 1023 K for 100 h. A: LSM in 3% H_2O/air, B and C: LSM in 3% H_2O/air in the presence of Cr vapor, D: LSCF in 3% H_2O/air, E/F: LSCF in 3% H_2O/air in presence of Cr vapor.

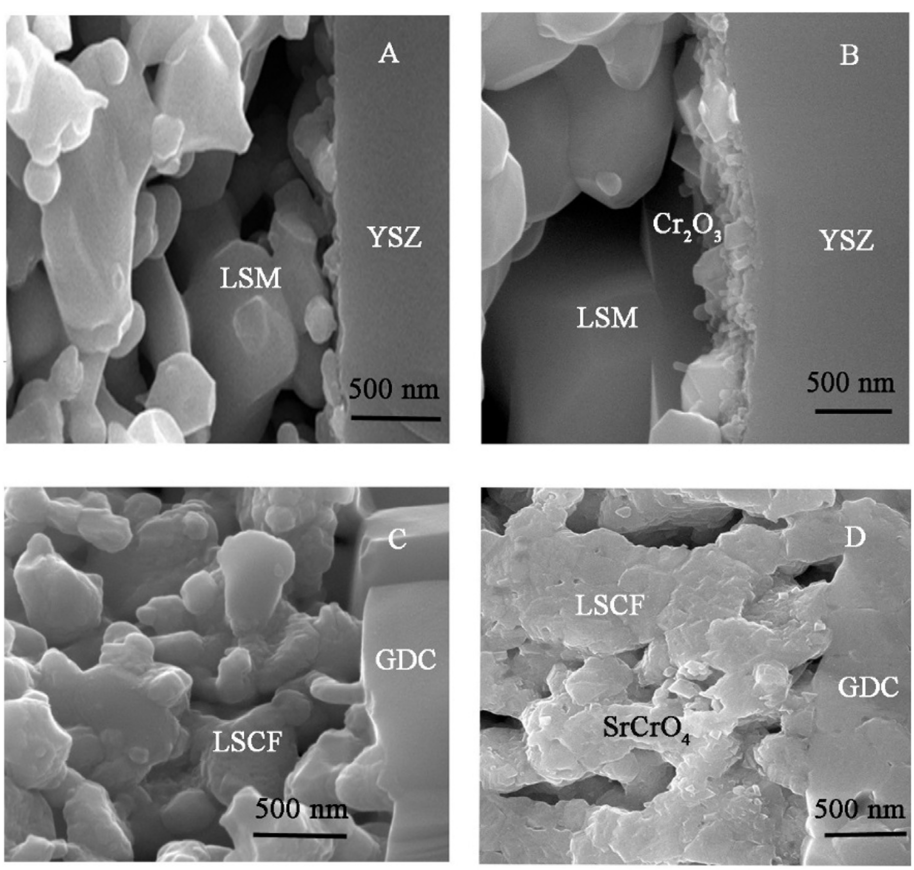

Fig. 5 – Fracture area analyses of LSM (LSCF)/YSZ (GDC) electrolyte in 3% H_2O/air in presence and absence of Cr vapor at 1023 K for 100 h. A: LSM/YSZ interface in 3% H_2O/air, B: LSM/YSZ in 3% H_2O/air in presence of Cr vapor, C: LSCF/GDC interface in 3% H_2O/air, D: LSCF/GDC interface in 3% H_2O/air and in absence of Cr.

Please cite this article in press as: Hu B, et al., Experimental and thermodynamic evaluation of $La_{1-x}Sr_xMnO_{3\pm\delta}$ and $La_{1-x}Sr_xCo_{1-y}Fe_yO_{3-\delta}$ cathodes in Cr-containing humidified air, International Journal of Hydrogen Energy (2017), http://dx.doi.org/10.1016/j.ijhydene.2017.01.040

Table 1 – Elemental analysis (selected area SEM-EDS) of LSM and LSCF cathode surfaces and cathode/electrolyte interfaces after half-cell tests in 3% H_2O/air for 100 h in the absence and presence of Cr vapor.

Element (%)	LSM cathode surface*	LSM cathode/ YSZ electrolyte	LSCF cathode surface	LSCF cathode/ GDC electrolyte#
CrK (atom%)	2.7 ± 0.2 (1.7 ± 0.1)	10.8 ± 0.5	13.1 ± 0.7	3.8 ± 0.2 (2.2 ± 0.1)
LaL (atom%)	37.0 ± 1.8 (37.9 ± 1.9)	23.9 ± 1.2	23.3 ± 1.2	27.6 ± 1.4 (28.0 ± 1.4)
SrK (atom%)	10.8 ± 0.5 (11.3 ± 0.6)	23.4 ± 1.2	23.6 ± 1.2	19.5 ± 1.0 (20.6 ± 1.0)
MnK (atom%)	49.4 ± 2.5 (49.1 ± 2.5)	41.9 ± 2.1	–	–
FeK (atom%)	–	–	31.5 ± 1.6	38.8 ± 1.9 (38.5 ± 1.9)
CoK (atom%)	–	–	7.8 ± 0.4	10.4 ± 0.5 (10.3 ± 0.5)

Note: "*" and "#": LSM and LSCF cathodes in absence of Cr, respectively.

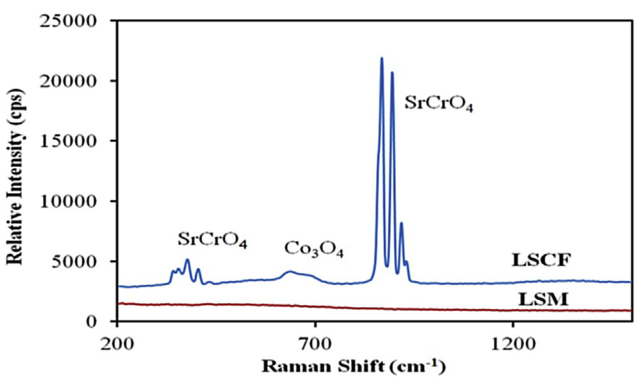

Fig. 6 – Raman spectra of post tested LSM and LSCF cathodes at 1023 K for 100-h tests in presence of chromium vapor.

stoichiometric LSM remains unreacted as $La_{0.75}Sr_{0.25}MnO_3$ for the entire range of experimental P_{CrO3} and temperature.

Discussion

Experimental observations show that LSM and LSCF cathodes exhibit two very different surface morphological evolutions and time dependent electrochemical performance degradation during exposure to chromium-containing humidified air atmosphere. The reaction process is schematically presented in Fig. 8 based on experimental and first-principles study that identifies thermodynamically favorable reaction products formation under experimental temperature and pressure conditions.

Strontium oxide segregation has been observed and confirmed by X-ray photoelectron spectroscopy on both LSM and LSCF cathode surfaces in earlier studies [41,42]. The segregation of SrO has also been found to increase with the water content, current density, and operating temperature [26]. Reversibly, the surface Sr species has also been found to be partially incorporated into the host lattice by cathodic activation [24,43]. In the presence of gaseous chromium species present in humidified air (point p, Fig. 7), segregated SrO present at the exposed surface of LSCF readily reacts with chromium vapor and converts to $SrCrO_4$ according to the reaction:

$$SrO_{(s)} + CrO_{3\,(g)} \rightarrow SrCrO_{4\,(s)} \quad (1)$$

General insights from the above energetics calculations also reveal that $La_{0.5}Sr_{0.5}CoO_3$ remains predominantly stable at low CrO_3 partial pressures and higher temperatures. However, at lower temperatures and with increase in CrO_3 partial pressures, a number of reaction products (Area 2) form. For $La_{0.75}Sr_{0.25}MnO_3$, on the other hand, absence of reaction products formation is evidenced under wide ranging experimental and SOFC operational conditions.

DFT calculations [39] show that SrO-terminated $LSCF_{113}$ has higher surface segregated Sr than the LSC_{113} (less Sr enriched termination). SrO, detected by energy ion

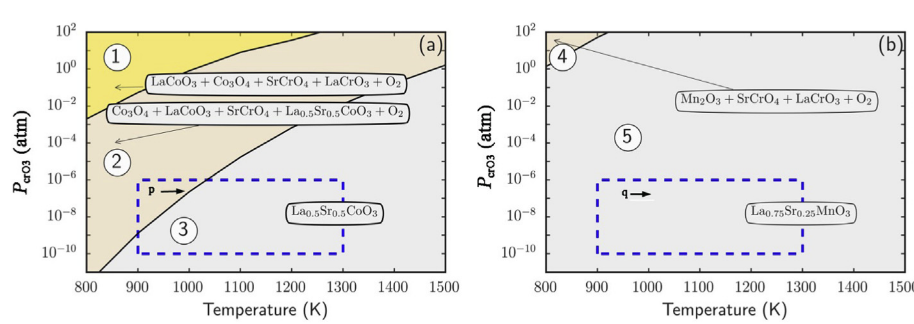

Fig. 7 – Phase field and reaction energetics of (a) $La_{0.5}Sr_{0.5}CoO_3$ (LSC) and (b) $La_{0.75}Sr_{0.25}MnO_3$ with CrO_3. The blue dashed rectangle shows the experimentally relevant range of P_{CrO3} and T. Points p and q show the locations of experimental conditions for this study for LSCF and LSM, respectively. (For interpretation of the references to color in this figure legend, the reader is referred to the web version of this article.)

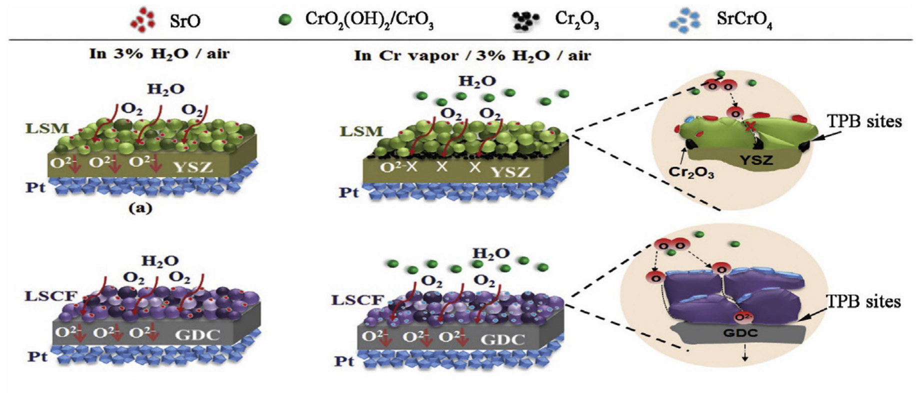

Fig. 8 – Illustration of the morphology evolution in the presence of water and chromium vapor.

scattering spectroscopy, is also reported to dominate the outer surfaces of LSCF cathode [44]. SEM observations (Fig. 4F) and Raman spectra (Fig. 6) on post tested LSCF samples show large amount of $SrCrO_4$ deposition during exposure to Cr-containing humidified air confirming the DFT predictions.

The amount of surface Sr segregation for LSCF and LSM is related to the strontium dopant concentration but more importantly, the termination sites determine the surface stability of the LSM and LSCF cathodes against oxide evolution and reaction products formation. Lowering of Sr concentration in LSCF from 0.4 to 0.3 reduced SrO segregation but could not eliminate Sr migration to the surface [45]. LSM lattice, on the other hand, is terminated by MnO_2 and SrO as found from first-principles studies [46]. A smooth LSM cathode surface observed on post tested samples (Fig. 4B/C) indicate largely MnO_2 and SrO termination leading to more chromium deposition resistant LSM surface compared to LSCF surface (Fig. 4E/F) which is terminated by SrO.

The difference in the ionic and electronic conductivity behavior of the LSCF and LSM also influences the surface chromium deposition pattern across the exposed cathode surface. A lower oxygen ion conductivity of LSM limits the oxygen reduction reactions (ORR) to the triple phase boundaries (TPB) between the electrode, electrolyte and O_2 [47]. Gas phase chromium species, which is not chemically adsorbed in the LSM cathode, is largely reduced to Cr_2O_3 (Cr^{3+}) and deposited at the LSM/YSZ interface (Fig. 8C) according to Reactions (2) and (3):

$$2CrO_{3\ (g)} \rightarrow Cr_2O_{3\ (s)} + 3/2O_{2\ (g)} + 6e^- \tag{2}$$

$$2CrO_2\ (OH)_{2\ (g)} \rightarrow Cr_2O_{3\ (s)} + 2H_2O_{\ (g)} + 3/2O_{2\ (g)} + 6e^- \tag{3}$$

It is noted that in the humidified air, reduction and deposition of chromium compounds from the hydrated gaseous species play dominant role due to their higher partial pressures. For LSCF cathode demonstrating mixed conducting (electronic and ionic conduction) behavior, oxygen reduction reaction not only takes place at the TPB (as in the case of LSM) but also at the free exposed surfaces in contact with the gas phase. The surface of the porous LSCF cathode traps most of the CrO_3 and $CrO_2(OH)_2$ vapors until saturated with chromium vapor. Un-trapped CrO_3 and $CrO_2(OH)_2$ can be further reduced at the extended TPB area near the cathode/electrolyte interface due to their excellent mixed ionic and electronic conductivity. The LSCF cathode, hence, shows improved resistance to chromium poisoning and only show minor electrochemical performance degradation as experimentally observed (Fig. 2) [48].

Conclusions

Chemical and structural stability of two typical cathodes LSM and LSCF have been compared using a combination of experimental evaluation and thermodynamic prediction approaches. The electrochemical performance of cathodes has been measured in the presence of gaseous chromium species present in humidified air (3% H_2O) using LSM/YSZ/Pt and LSCF/GDC/Pt half-cells at 1023 K. During the 100-h electrochemical tests, the LSM/YSZ/Pt half-cell exhibited a rapid decrease in the current density with time while the LSCF/GDC/Pt half-cell exhibited only a slight decrease in current density. SEM-EDS images revealed that Cr species deposited mainly at LSM/YSZ interface while Cr deposited mainly at LSCF surface. Raman spectra show $SrCrO_4$ formation on the post tested LSCF cathode but not on the post tested LSM cathode. The polarization resistance of the LSM cathode showed larger increase than that of the LSCF cathode in the presence of gaseous Cr containing air.

A linear programming approach coupled with first-principles thermodynamic analysis was employed to identify the decomposition products and reaction energetics of $La_{0.75}Sr_{0.25}MnO_3$ and $La_{0.5}Sr_{0.5}CoO_3$ compounds in the presence of Cr vapor. The bulk reaction energetics suggests that the stoichiometric LSM remains unreacted for the range of experimental P_{CrO3} and temperature conditions whereas the formation of $SrCrO_4$ on $La_{0.5}Sr_{0.5}CoO_3$ cathode is energetically favored at 1023 K. Experimental results support theoretical calculations.

Please cite this article in press as: Hu B, et al., Experimental and thermodynamic evaluation of $La_{1-x}Sr_xMnO_{3\pm\delta}$ and $La_{1-x}Sr_xCo_{1-y}Fe_yO_{3-\delta}$ cathodes in Cr-containing humidified air, International Journal of Hydrogen Energy (2017), http://dx.doi.org/10.1016/j.ijhydene.2017.01.040

Acknowledgements

We acknowledge the financial support from US Department of Energy and National Energy Technological Laboratory under federal grant DE-FE 0023385. Technical discussions with Dr. Jeff Stevenson (PNNL) and Dr. Patcharin Burke (NETL) are gratefully acknowledged. We thank the Center for Clean Energy Engineering, University of Connecticut for providing the instruments and facilities for the timely execution of experimental work.

REFERENCES

[1] Chen X, Zhen Y, Li J, Jiang SP. Chromium deposition and poisoning in dry and humidified air at $(La_{0.8}Sr_{0.2})_{0.9}MnO_{3+\delta}$ cathodes of solid oxide fuel cells. Int J Hydrogen Energy 2010;35:2477–85.

[2] Yang Z, Xia GG, Walker MS, Wang CM, Stevenson JW, Singh P. High temperature oxidation/corrosion behavior of metals and alloys under a hydrogen gradient. Int J Hydrogen Energy 2007;32:3770–7.

[3] Ge L, Verma A, Goettler R, Lovett D, Raman RKS, Singh P. Oxide scale morphology and chromium evaporation characteristics of alloys for balance of plant applications in solid oxide fuel cells. Metall Mater Trans A 2013;44:193–206.

[4] Harikishan RE, Iain S, Piotr B, Bruno GP, Sivakumar P. Current status of fuel cell based combined heat and power systems for residential sector. J Power Sources 2015;293:312–28.

[5] Yu B, Zhang W, Xu J, Chen J. Status and research of highly efficient hydrogen production through high temperature steam electrolysis at INET. Int J Hydrogen Energy 2010;35:2829–35.

[6] Wang Z, Mori M, Araki T. Steam electrolysis performance of intermediate-temperature solid oxide electrolysis cell and efficiency of hydrogen production system at 300 Nm^3/h. Int J Hydrogen Energy 2010;35:4451–8.

[7] Li Q, Zheng Y, Guan W, Jin L, Xu C, Wang WG. Achieving high-efficiency hydrogen production using planar solid-oxide electrolysis stacks. Int J Hydrogen Energy 2014;39:10833–42.

[8] Guan W, Jin L, Wu W, Zheng Y, Wang G, Wang WG. Effect and mechanism of Cr deposition in cathode current collecting layer on cell performance inside stack for planar solid oxide fuel cells. J Power Sources 2014;245:119–28.

[9] Li Y, Gemmen R, Liu X. Oxygen reduction and transportation mechanisms in solid oxide fuel cell cathodes. J Power Sources 2010;195:3345–58.

[10] Williford RE, Singh P. Engineered cathodes for high performance SOFCs. J Power Sources 2004;128:45–53.

[11] Kozuka H, Yamagiwa K, Ohbayashi K, Koumoto K. Origin of high electrical conductivity in alkaline-earth doped $LaCoO_3$. J Mater Chem 2012;22:11003–5.

[12] Singh P, Vasilow T, Richards VL. Protective interlayer for high temperature solid electrolyte electrochemical cells. Pittsburgh, PA: US: Westinghouse Electric Corporation; 1996. NETL.

[13] Zhao L, Kong JDC, Amarasinghe S, Jiang SP. Insight into surface segregation and chromium deposition on $La_{0.6}Sr_{0.4}Co_{0.2}Fe_{0.8}O_{3-\delta}$ cathodes of solid oxide fuel cells. J Mater Chem A 2014;2:11114–23.

[14] Nguyen VN, Fang Q, Packbier U, Blum L. Long-term tests of a Juelich planar short stack with reversible solid oxide cells in both fuel cell and electrolysis modes. Int J Hydrogen Energy 2013;38:4281–90.

[15] Jin T, Lu K. Chemical compatibility between Sr-doped lanthanum manganite air electrode and AISI 441 interconnect. Int J Hydrogen Energy 2011;36:4440–8.

[16] Kornely M, Menzler NH, Weber A, Ivers-Tiffée E. Degradation of a high performance SOFC cathode by Cr-poisoning at OCV-conditions. Fuel Cells 2013;13:506–10.

[17] Norbert HM, Vinke I, Hannelore L. Chromium poisoning of LSM cathodes – results from stack testing. ECS Trans 2009;25:2899–908.

[18] Nielsen J, Hagen A, Liu YL. Effect of cathode gas humidification on performance and durability of solid oxide fuel cells. Solid State Ionics 2010;181:517–24.

[19] Liu RR, Kim SH, Taniguchi S, Oshima T, Shiratori Y, Ito K, et al. Influence of water vapor on long-term performance and accelerated degradation of solid oxide fuel cell cathodes. J Power Sources 2011;196:7090–6.

[20] Caillol N, Pijolat M, Siebert E. Investigation of chemisorbed oxygen, surface segregation and effect of post-treatments on $La_{0.8}Sr_{0.2}MnO_3$ powder and screen-printed layers for solid oxide fuel cell cathodes. Appl Surf Sci 2007;253:4641–8.

[21] Simner SP, Anderson MD, Engelhard MH, Stevenson JW. Degradation mechanisms of La-Sr-Co-Fe-O_3 SOFC cathodes. Electrochem Solid-State Lett 2006;9:478–81.

[22] Komatsu T, Chiba R, Arai H, Sato K. Chemical compatibility and electrochemical property of intermediate-temperature SOFC cathodes under Cr poisoning condition. J Power Sources 2008;176:132–7.

[23] Schuler JA, Wuillemin Z, Hessler-Wyser A, Comminges C, Steiner NY, Herle JV. Cr-poisoning in (La,Sr)(Co,Fe)O_3 cathodes after 10,000 h SOFC stack testing. J Power Sources 2012;211:177–83.

[24] Hu B, Mahapatra MK, Keane M, Zhang H, Singh P. Effect of CO_2 on the stability of strontium doped lanthanum manganite cathode. J Power Sources 2014;268:404–13.

[25] Darvish S, Asadikiya M, Hu B, Singh P, Zhong Y. Thermodynamic prediction of the effect of CO_2 to the stability of $(La_{0.8}Sr_{0.2})_{0.98}MnO_{3\pm\delta}$ system. Int J Hydrogen Energy 2016;41:10239–48.

[26] Hu B, Keane M, Mahapatra MK, Singh P. Stability of strontium-doped lanthanum manganite cathode in humidified air. J Power Sources 2014;248:196–204.

[27] Hu B, Mahapatra MK, Singh P. Performance regeneration in lanthanum strontium manganite cathode during exposure to H_2O and CO_2 containing ambient air atmospheres. J Ceram Soc Jpn 2015;123:1–6.

[28] Meschter PJ, Opila EJ, Jacobson NS. Water vapor–mediated volatilization of high-temperature materials. Annu Rev Mater Res 2013;43:559–88.

[29] Chen X, Jin C, Zhao L, Zhang L, Guan C, Wang L, et al. Study on the Cr deposition and poisoning phenomenon at $(La_{0.6}Sr_{0.4})(Co_{0.2}Fe_{0.8})O_{3-\delta}$ electrode of solid oxide fuel cells by transmission x-ray microscopy. Int J Hydrogen Energy 2014;39:15728–34.

[30] Jiang SP, Chen X. Chromium deposition and poisoning of cathodes of solid oxide fuel cells – a review. Int J Hydrogen Energy 2014;39:505–31.

[31] Liu DJ, Almer J, Cruse T. Characterization of Cr poisoning in a solid oxide fuel cell cathode using a high energy X-ray microbeam. J Electrochem Soc 2010;157:744–50.

[32] Bucher E, Yang M, Sitte W. *In situ* investigations of the chromium-induced degradation of the oxygen surface exchange kinetics of IT-SOFC cathode materials $La_{0.6}Sr_{0.4}CoO_{3-\delta}$ and $La_{0.58}Sr_{0.4}Co_{0.2}Fe_{0.8}O_{3-\delta}$. J Electrochem Soc 2012;159:592–6.

[33] Zhao L, Zhang J, Becker T, Jiang SP. Raman spectroscopy study of chromium deposition on $La_{0.6}Sr_{0.4}Co_{0.2}Fe_{0.8}O_{3-\delta}$ cathode of solid oxide fuel cells. J Electrochem Soc 2014;161:687–93.

[34] Lee SN, Atkinson A, Kilner JA. Effect of chromium on $La_{0.6}Sr_{0.4}Co_{0.2}Fe_{0.8}O_{3-\delta}$ solid oxide fuel cell cathodes. J Electrochem Soc 2013;160. F629–F35.
[35] Akbarzadeh AR, Wolverton C, Ozolins V. First-principles determination of crystal structures, phase stability, and reaction thermodynamics in the Li-Mg-Al-H hydrogen storage system. Phys Rev B 2009;79(184102):1–10.
[36] Duan Y, Zhang B, Sorescu DC, Johnson JK. CO_2 capture properties of M–C–O–H (M=Li, Na, K) systems: a combined density functional theory and lattice phonon dynamics study. J Solid State Chem 2011;184:304–11.
[37] Kresse G, Furthmuller J. Efficiency of ab-initio total energy calculations for metals and semiconductors using a plane-wave basis set. Comput Mat Sci 1996;6:15–50.
[38] Perdew JP, Burke K, Ernzerhof M. Generalized gradient approximation made simple. Phys Rev Lett 1996;77:3865–8.
[39] Krishnan S, Sharma V, Singh P, Ramprasad R. Dopants in lanthanum manganite: insights from First-principles chemical space exploration. J Phys Chem C 2016;120:22126–33.
[40] Lee SH, Huh YD. Preparation of ultralong $SrCrO_4$ nanowires by a surfactant-free solvothermal reaction. Bull Korean Chem Soc 2013;34:1921–3.
[41] Huber A, Falk M, Rohnke M, Luerssen B, Amati M, Gregoratti L, et al. *In situ* study of activation and de-activation of LSM fuel cell cathodes – electrochemistry and surface analysis of thin-film electrodes. J Catal 2012;294:79–88.
[42] Jalili H, Han J, Kuru Y, Cai Z, Bilge Y. New Insights into the strain coupling to surface chemistry, electronic structure, and reactivity of $La_{0.7}Sr_{0.3}MnO_3$. J Phys Chem Lett 2011;2:801–7.
[43] Pan Z, Liu Q, Zhang L, Zhang X, Chan SH. Effect of Sr surface segregation of $La_{0.6}Sr_{0.4}Co_{0.2}Fe_{0.8}O_{3-\delta}$ electrode on its electrochemical performance in SOC. J Electrochem Soc 2015;162:1316–23.
[44] Druce J, Tellez H, Burriel M, Sharp MD, Fawcett LJ, Cook SN, et al. Surface termination and subsurface restructuring of perovskite-based solid oxide electrode materials. Energy Environ Sci 2014;7:3593–9.
[45] Yu Y, Ludwig KF, Woicik JC, Gopalan S, Pal UB, Kaspar TC, et al. Effect of Sr content and strain on Sr segregation of $La_{1-x}Sr_xCo_{0.2}Fe_{0.8}O_{3-\delta}$ as cathode material for solid oxide fuel cells. ACS Appl Mater Interfaces 2016;8:26704–11.
[46] Piskunov S, Jacob T, Spohr E. Oxygen adsorption at $La_{1-x}Sr_xMnO_3$ (001) surfaces: predictions from first-principles. Phys Rev B Condens Matter 2011;83(073402):1–4.
[47] Jiang SP, Wang W. Novel structured mixed ionic and electronic conducting cathodes of solid oxide fuel cells. Solid State Ionics 2005;176:1351–7.
[48] Matsuzaki Y, Yasuda I. Dependence of SOFC cathode degradation by chromium-containing alloy on compositions of electrodes and electrolytes. J Electrochem Soc 2001;148:126–31.